Journal of Carbon Research

MDPI

Article

Biographite from Wood—Surpassing Structural Limitations by Catalytic Graphitization Using Iron Sulfate Salts

Sabrina Schmid [1], Rene Zahrhuber [2], Neda Nazari [1,2], Andrei Ionut Mardare [3,4], Christian Fürst [1], Achim Walter Hassel [3,5], Igor A. Pašti [6,7], David Stifter [2] and Christoph Unterweger [1,*]

1 Wood K Plus—Kompetenzzentrum Holz GmbH, Altenberger Strasse 69, 4040 Linz, Austria; s.schmid@wood-kplus.at (S.S.); n.nazari@wood-kplus.at (N.N.); c.fuerst@wood-kplus.at (C.F.)
2 Center for Surface and Nanoanalytics (ZONA), Johannes Kepler University (JKU) Linz, Altenberger Strasse 69, 4040 Linz, Austria; rene.zahrhuber@jku.at (R.Z.); david.stifter@jku.at (D.S.)
3 Institute of Chemical Technology of Inorganic Materials, Johannes Kepler University (JKU) Linz, Altenberger Strasse 69, 4040 Linz, Austria; andrei.mardare@jku.at (A.I.M.); achimwalter.hassel@jku.at (A.W.H.)
4 National Institute for Lasers, Plasma and Radiation Physics, 077125 Magurele, Romania
5 Faculty of Medicine and Dentistry, Danube Private University, Steiner Landstrasse 124, 3500 Krems an der Donau, Austria
6 Faculty of Physical Chemistry, University of Belgrade, Studentski trg 12-16, 11158 Belgrade, Serbia; igor@ffh.bg.ac.rs
7 Serbian Academy of Sciences and Arts, Kneza Mihaila 35, 11000 Belgrade, Serbia
* Correspondence: c.unterweger@wood-kplus.at; Tel.: +43-676-897-44-534

Abstract

Biomass serves as an abundant carbon feedstock, yet its inherently "non-graphitizable" nature typically limits its use in high-performance applications such as batteries and electronics. This study investigates the catalytic graphitization of wood dust using iron(II) sulfate (IS) and ammonium-iron(II) sulfate (AIS) as scalable, non-toxic alternatives to traditional metal catalysts such as Ni, Co or Mo. Wood powder was impregnated with aqueous solutions of these Fe salts and carbonized at temperatures ranging from 900 °C to 2200 °C, followed by structural and electrical characterization using XRD, Raman spectroscopy, gas adsorption, and four-point probe resistance measurements. Results demonstrate that both Fe salts successfully induced high-order graphitic regions at temperatures as low as 1100 °C, achieving interlayer spacing (~0.336 nm) close to perfect graphite, while non-impregnated wood remained poorly ordered even at 2200 °C with interlayer spacing that can be associated with turbostratic structures. This improved structural ordering is also reflected in the electrical conductivity of the catalytically graphitized samples, which is competitive with commercial graphite already at production temperatures as low as 1300 °C. Additionally, in the medium temperature range around 1500 °C, the catalytically graphitized samples show unique combinations of high conductivity and large specific surface area (up to 586 m^2 g^{-1}). These findings show that iron salts are effective, sustainable catalysts for transforming biomass into high-quality graphitic carbon at significantly reduced process temperatures.

Keywords: graphite; catalytic graphitization; sustainability; biomass; iron salt

Check for updates

Academic Editor: Sergey Mikhalovsky

Received: 9 September 2026
Revised: 6 October 2026
Accepted: 10 October 2026
Published: 15 October 2026

Copyright: © 2026 by the authors. Licensee MDPI, Basel, Switzerland. This article is an open access article distributed under the terms and conditions of the Creative Commons Attribution (CC BY) license.

1. Introduction

Natural graphite has been classified as a critical raw material by the European Union due to its use in batteries and as refractories for steelmaking [1]. Almost all synthetic graphite is produced from fossil carbon sources at high temperatures [2–4]. Graphite and graphitic carbons show useful properties such as high chemical stability [5] and

high thermal and electrical conductivities [3], depending on the feedstock, process and operating conditions [6]. These properties make them valuable, not only for batteries [7–9] and refractories for steelmaking [10] but also for graphene production through mechanical or chemical exfoliation [11,12], as conductivity additives, for example, in supercapacitors [13,14] or printed electronics [15,16] or as lubricants [10]. Biomass, such as wood, is abundant in Europe and offers a promising carbon feedstock. A high carbon content as well as low costs are important considerations for a commercial-scale production [3]. However, biomass-derived carbon is typically "non-graphitizable" under conventional high-temperature treatments [5,6,17]. To a certain extent, "non-graphitizable" carbons also graphitize [18], but even at extremely high temperatures (e.g., 2800 °C), no sufficient graphitic order with interlayer spacing close to that of perfect graphite and larger crystallite sizes can be achieved, limiting their applicability in high-performance materials [6,19,20].

Catalytic graphitization has emerged as a transformative approach to overcome this limitation. By introducing metal catalysts, graphitic structures can be formed from "non-graphitizable" precursors. Interlayer spacing can be significantly reduced and crystallite sizes increased to values comparable to natural graphite. Additionally, process temperatures can be significantly reduced [5]. Many studies actually focus on the development of graphitic structures or preparation of electrically conducting carbons at low temperatures [21,22], with some even stating temperatures as low as 715 °C [23]. While the precursor also plays an essential role in the structure of the final carbons [24], with wood, cellulose and lignin being the most widely used materials [23,25–27], the main impact factor is the catalyst and how it is introduced in the precursor material. Typically, (transition-) metal salts, such as Ni, Co, Cu, Mo, Fe and Ca as well as multi-metal catalysts are described [3,11,28,29]. Fe, in particular, has been widely studied for its catalytic efficiency, non-toxic nature, availability, and cost-effectiveness [22,23,25–27,30,31]. For Fe-based catalysts, two main mechanisms are discussed in the literature, dissolution/precipitation and carbide formation/decomposition. Both describe the formation of highly ordered domains around Fe particles [3]. However, a recent study discovered a new mechanism of burrowing through amorphous carbon to generate multiwalled graphitic nanotubes called "homogeneous solid-state catalysis" [32]. Higher iron loadings lead to a higher degree of graphitization [24,33]. Particle size and particle distribution additionally influence the graphitization process [33]. Dissolution of the metal salts and wet impregnation ensure the best catalyst distribution within the feedstock matrix. Previous research has primarily focused on iron nitrate salts, which can pose scalability challenges. Alternative iron-based catalysts could include iron(II)sulfate (IS) and ammonium-iron(II)sulfate (AIS). Both are highly soluble in water, which makes them ideal for impregnation. In addition, AIS might also have a beneficial effect on the carbon yield similar to ammonium sulfate that has been previously used as a cellulose dehydration catalyst in the thermal conversion of cellulose/lignin filaments [34]. Both iron salts represent scalable and safe alternatives to nitrates, yet their potential for catalytic graphitization of biomass has remained largely unexplored.

This study systematically investigates catalytic graphitization of wood using IS and AIS. The process is conducted at various temperatures to investigate how the process temperature influences structure formation. This study focuses on a scalable, simple solution for the catalytic graphitization of wood in order to demonstrate a method for processing larger quantities. By optimizing the process parameters, we aim to contribute to the development of sustainable, high-performance carbon materials derived from biomass, thereby reducing dependence on natural and fossil-based synthetic graphite.

2. Materials and Methods

Arbocel CW630PU wood powder was purchased from J. Rettenmaier & Söhne (Rosenberg, Germany) and dried in a cabinet dryer at 105 °C for 8 h. It was separated into three parts, and two were impregnated with 1 M solutions of iron(II)-sulfate heptahydrate (IS; CAS: 7782-63-0) and ammonium-iron(II)-sulfate hexahydrate (AIS; CAS: 7783-85-9) respectively, all purchased from Carl Roth (Karlsruhe-Mühlburg, Germany). Precursor and catalyst solution were mixed for 30 s using an Ultraturrax (IKA-Werke, Staufen, Germany) and centrifuged to separate the liquid phase. After drying at 70 °C overnight, the samples were carbonized at 900 °C using an HTK 8 W chamber furnace (Carbolite Gero, Neuhausen, Germany), together with the third pristine part. After evacuation of the chamber, a nitrogen flow of 250 L h^{-1} was adjusted. The sample was heated using a temperature program (5 °C min^{-1} to 180 °C, 1 °C min^{-1} to 400 °C, 5 °C min^{-1} to 900 °C) and held at 900 °C for 30 min. Subsequent thermal treatment steps were conducted with the materials carbonized at 900 °C. A heating ramp of 5 °C min^{-1} to the final temperature was used, followed by an isothermal holding step for 30 min. A flow rate of 250 L h^{-1} of inert gas was used—N_2 for thermal treatments at 1100 °C, 1300 °C and 1500 °C and Ar for 2000 °C and 2200 °C.

To remove iron residues from the prepared carbons, washing with concentrated hydrochloric acid (37%, CAS: 7647-01-0, purchased from Merck, Darmstadt, Germany) was performed. A total of 500 mg of each sample was added to 20 mL of hydrochloric acid, mixed using an ultrasonic bath and stored overnight. The samples were filtered using a sintered glass funnel Por.4, and 80 mL of deionized water was added and adjusted to a pH value of 7 using a 0.1 N NaOH solution (prepared from sodium hydroxide, CAS: 1310-73-2, purchased from Carl Roth, Karlsruhe-Mühlburg, Germany), if applicable. The samples were stored overnight, while some of them became acidic again. Those samples were again filtered, washed using deionized water and stored overnight. Washing with water was repeated until the samples became neutral, and they were then filtered and dried using a drying cabinet at 160 °C overnight.

The iron loading of the samples [g Fe/g wood] was determined gravimetrically immediately after impregnation using Equation (1), where m is the mass of the wet impregnated sample, m_0 is the mass of the dried wood powder before impregnation, c refers to the concentrations of the impregnation solutions (24.4 wt.% for IS and 32.7 wt.% for AIS determined by weight measurements), RM is the residual moisture content of the dried wood powder, M is the molar mass of iron and M_{tot} is the molar mass of IS or AIS.

$$Fe\ Loading = \frac{(m - m_0) \cdot c \cdot M}{m_0 \cdot (1 - RM) \cdot M_{tot}} \quad (1)$$

The actual iron loading of the IS-impregnated samples was 18.5%, while it was 18.9% for the AIS-impregnated samples. For comparison, commercial graphite C-nergy KS-L (Imerys, Paris, France) was used.

Raman spectra were recorded by using a Horiba Scientific (Kyoto, Japan) LabRam Aramis Raman microscope. A Nd:YAG laser with a wavelength of 532 nm, a diffraction grating of 300 grooves/mm, and a Peltier-cooled CCD detector were chosen for operation. The beam was focused with a 100× magnification objective, which allows a focal point of roughly 1 µm in diameter. Calibration of the instrument was done against the Stokes Raman signal of pure silicon at 520 cm^{-1} using a silicon wafer (111) crystal plane surface. Spectra were recorded in the Stokes region from 100 to 3500 cm^{-1} and the baseline was corrected using the "goldindec" algorithm approach [35]. "Goldindec" is an automated Raman spectrum baseline correction algorithm designed to separate broad fluorescence/background signals from narrow Raman peaks. It models the baseline with a low-order polynomial and

iteratively refines the fit by identifying spectral points that are likely to belong to Raman peaks and reducing their influence on the polynomial regression.

Peak fitting of the D and G bands was done using Lorentzian models at around 1345 cm^{-1} and 1590 cm^{-1}. The other first-order bands, namely D4, D3 and D2, were deconvoluted using Lorentzian models at 1150 cm^{-1}, 1500 cm^{-1} and 1610 cm^{-1} respectively, if applicable. The second-order spectrum was deconvoluted into three further peaks also using Lorentzian models at around 2650 cm^{-1}, 2930 cm^{-1} and 3200 cm^{-1}.

X-ray diffraction (XRD) was measured using an Ultima IV diffractometer (Rigaku Corporation, Tokyo, Japan) with a Ni-filtered Cu Kα radiation source (λ = 1.5406 Å). The crystallographic data were collected in Bragg–Brentano mode, in the 2θ range from 3 to 90° with a scan step size of 0.05°. XRD spectra were baseline-corrected manually, and the (002) diffraction peaks were fitted with either one or two pseudo-Voigt functions, depending on whether a sharp peak around 26° was present [2]. For fitting, the Fityk 1.3.1 software was used. Only data points between 13° and 35° were used for fitting; all others were set to inactive. The baseline was set manually, with several points before and after the (002) peak, always including points at 15° and 33°. The resulting functions were analyzed regarding their peak maximum θ_{002} and the full width at half maximum (FWHM, β) [19]. The interlayer spacing d_{002} was determined using Bragg's law:

$$d_{002} = \frac{n \cdot \lambda}{2 \cdot \sin(\theta_{002})} \quad (2)$$

where n is the integer (usually 1) and λ is the Cu-Kα radiation wavelength with 1.5406 Å. The crystallite size *Lc* was calculated using the Scherrer equation:

$$Lc = \frac{K \cdot \lambda}{\beta \cdot \cos \theta_{002}} \quad (3)$$

where K is a dimensionless constant of 0.89. Fitting and subsequent calculations were done three times, and the average value and the 0.95 confidence interval were calculated to address fitting uncertainty. The average number of stacked graphene fringes $n_{fringes}$ was calculated by dividing the average crystallite size by the average interlayer spacing:

$$n_{fringes} = \frac{Lc}{d_{002}} + 1 \quad (4)$$

Electrical resistivity was measured using a SDKR-13 4-point probe (Nagy Messsysteme GmbH, Gäufelden-Nebringen, Germany) with spring-loaded Rh-plated steel needles (250 µm tip diameter) spaced at 1.3 mm. The obtained uniform force applied to each needle is approximately 1 N. A total of 144 mg of each carbon sample (or the graphite reference) was mixed with 16 mg of PTFE powder (PTFE with a mean particle size of 20 µm; Sigma Aldrich, St. Louis, MO, USA) and kneaded using mortar and pestle until a kneadable dough was obtained. The dough was processed to a carbon–PTFE foil with at least 25 × 25 mm^2 having a maximum thickness of 150 µm using a sheet metal roller [36]. The resistivity ρ [Ω cm] was calculated according to Valdes, where V is the floating potential difference between the inner probes, I is the current through the outer pare of probes and s is the needle distance [37]:

$$\rho = \frac{V}{I} 2\pi s \quad (5)$$

Subsequently, the sheet resistance R [Ω/sq] was calculated by dividing the resistivity by the thickness of the foil. Each carbon–PTFE foil was measured 12 times, and the average value calculated.

N_2 adsorption at an isothermal temperature of −196.15 °C was used in a gas sorption system (Autosorb-iQ, Anton Paar QuantaTec Inc., Graz, Austria) to examine the porosity of the samples. The samples were outgassed for 3 h at 300 °C under vacuum before analysis. A multi-point BET approach was used to determine the specific surface area, while the pore volume was estimated to be equal to the liquid volume of the N_2 adsorbate at a relative pressure of 0.99.

Morphological analysis of the carbonized wood samples was conducted with a CrossBeam 1540 XB FIB-SEM (Carl Zeiss AG, Oberkochen, Germany). Secondary electron imaging was used to distinguish phases, offering superior resolution and improved signal-to-noise ratios. Three-dimensional characterization of the boundary region was performed by FIB tomography using Ga ions at 10 kV.

X-ray photoelectron spectroscopy (XPS) measurements were carried out on a Thermo Fisher Scientific Nexsa G2 system (Waltham, MA, USA) operated in standard lens mode and at constant analyzer energy (CAE). A monochromated Al-Kα X-ray source ($h\nu$ = 1486.6 eV) was used for excitation. Survey spectra were recorded with a pass energy of 200 eV and an energy step of 1.0 eV (dwell time 50 ms). High-resolution spectra were acquired with pass energies of 20 eV using an energy step of 0.05 eV and a dwell time of 50 ms to ensure high intensity at a suitable signal-to-noise ratio. For large-area measurements, the X-ray spot was set to 400 µm in diameter to balance depth resolution, spectral quality, and acquisition time. Surface charging was compensated using the instrument's dual flood gun, which simultaneously supplies low-energy electrons and Ar ions to the sample surface. Unless otherwise stated, charge referencing was performed using the C_{1s} peak of adventitious carbon at 284.8 eV. Data acquisition and quantification were performed with the manufacturer's Avantage software v6.8.0. Background subtraction employed the Smart background (a modified Shirley), and Scofield sensitivity factors were used for elemental quantification.

The authors used ChatGPT to prepare the Graphical Abstract. The authors manually modified and rearranged the images and added their own figures. The final Graphical Abstract was assembled and revised by the authors. The authors have reviewed and edited the output and take full responsibility for the content of this publication.

3. Results and Discussion

In this study, wood dust was used as a precursor and IS and AIS were evaluated as graphitization catalysts. Besides the testing of rarely used iron sulfate catalysts, the main aim was the evaluation of the graphitization temperature in the range of 900 to 2200 °C. To minimize the influence of iron loadings and have more focus on the different processing temperatures, a relatively high iron content was desired. Based on similar studies using concentrations of 0.25–2 M [23,27,38] and our own preliminary screenings, 1 M solutions were chosen to achieve sufficient iron loadings.

3.1. XRD

The crystallographic structure of the samples at different carbonization temperatures was determined using XRD and compared to commercial graphite. The general shape of the diffractograms gives information about the quality and quantity of graphitization. All samples carbonized at 900 °C show broad symmetric peaks typical for low-ordered structure. However, both iron-impregnated samples already show narrower peaks shifted to slightly higher 2θ values, indicating higher structural order compared to the non-impregnated reference sample. Starting at 1100 °C, asymmetric peaks were detected for both iron-impregnated samples. In Figure 1a, diffractograms of graphite and wood samples carbonized at 1300 °C are compared. Commercial graphite possesses a very sharp (002) peak at 26.4°, which is attributed to an interlayer spacing d_{002} of 0.337 nm, which is very close to

the theoretical literature value of 0.3354 nm [39,40]. The (002) peak of the non-impregnated sample (wood 1300 °C) is much broader, indicating poor structural order with small crystallite sizes or high curvature of the graphene fringes [2]. It is additionally shifted to a lower 2θ value due to higher interlayer spacing, as described for immature carbons [39]. Both iron-impregnated samples (wood + AIS and wood + IS) show an asymmetric (002) peak with a broader part, shifted to a lower 2θ value, and a sharper part exactly at 26.4°. This sharper peak indicates high-order graphitic regions within low-order regions described before [2]. To evaluate asymmetric (002) peaks, two curves were used to fit low-order regions (LOR) and high-order regions (HOR), as presented in Figure 1b. Both fittings were evaluated regarding their interlayer spacing. HOR peaks of all iron-impregnated carbon samples show interlayer spacings below 0.340 nm. These values are below the interlayer spacings reported for turbostratic carbon, for which a limit of 0.344 nm or even higher, depending on local steric constraints, has been reported [39]. Non-impregnated reference samples show HOR peaks only at carbonization temperatures higher than 2000 °C, with interlayer spacings close to those of turbostratic carbon. They show (10) and (11) peaks, which are broad and asymmetric, typical for turbostratic carbon. The broadness of the peaks indicates small crystallite sizes and/or curvature of the graphene fringes [2] as well as random orientation of the stacks. Other graphitic peaks displayed here are (100), (101), (004), (110) and (112), coming from its hexagonal structure. Some of them are slightly visible in the iron-impregnated samples, starting from a graphitization temperature of 1300 °C, e.g., (110) and (112) of the iron-impregnated samples wood + IS 1300 °C and wood + AIS 1300 °C (Figure 1a), depending on the quality of the XRD measurement. Even a slight segregation of the (10) peak into two separate peaks is visible. These results indicate the formation of graphitic structures through impregnation with iron salts, which are not visible in the non-impregnated reference samples.

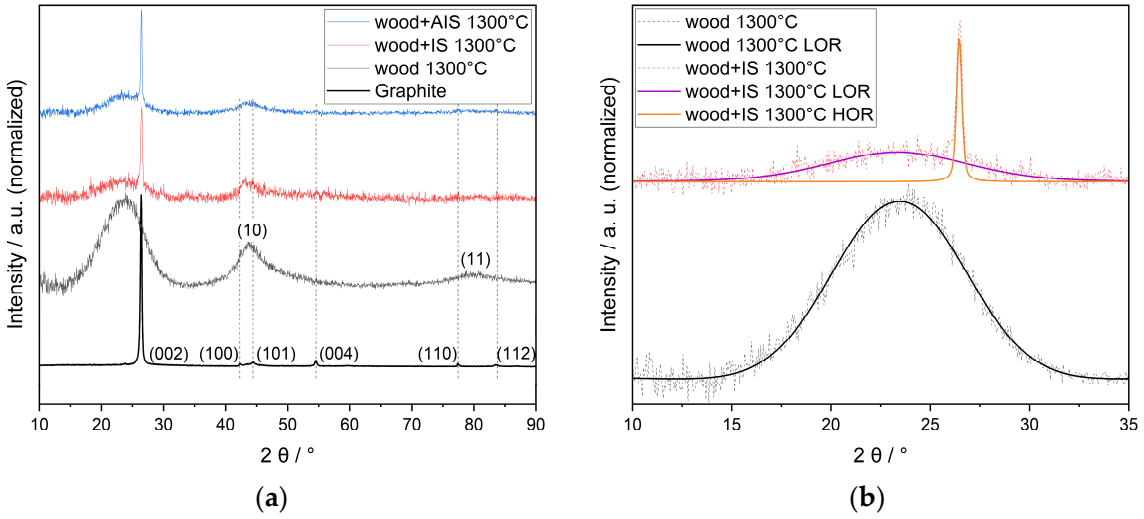


Figure 1. XRD diffractograms of (**a**) graphite and Fe-impregnated and non-impregnated wood samples carbonized at 1300 °C and (**b**) non-impregnated and IS-impregnated wood samples carbonized at 1300 °C, including (002) peak fittings.

Figure 2 shows the evolution of the IS-impregnated wood dust with increasing temperature. At 900 °C, no (002) HOR peak is visible, while at 1100 °C, a small peak can already be seen. The calculation of the interlayer spacing for the HOR already shows a value of 0.336 nm, attributed to a fully graphitic structure. With increasing temperature, the (002) HOR peak increases, until at 2000 °C and 2200 °C, only an HOR and no LOR peak can be fitted. All other peaks attributed to a graphitic structure also increase with increasing temperature. According to Monthioux, a (112) diffraction peak ascertains a graphitic or

partially graphitic structure [41]. Diffractograms at 2000 °C and 2200 °C exhibit Fe impurities (indicated by *) despite excessive washing with concentrated hydrochloric acid and water. We assume a certain iron particle enclosure within graphitic shells, as the literature describes the formation of graphitic structures around the catalyst particles [42]. At higher carbonization temperatures, iron particles sinter together, leading to larger particles with a higher average number of graphene sheets [42]. Therefore, graphitic shells are thicker and neater, which makes washing more complex, leading to residual iron impurities.

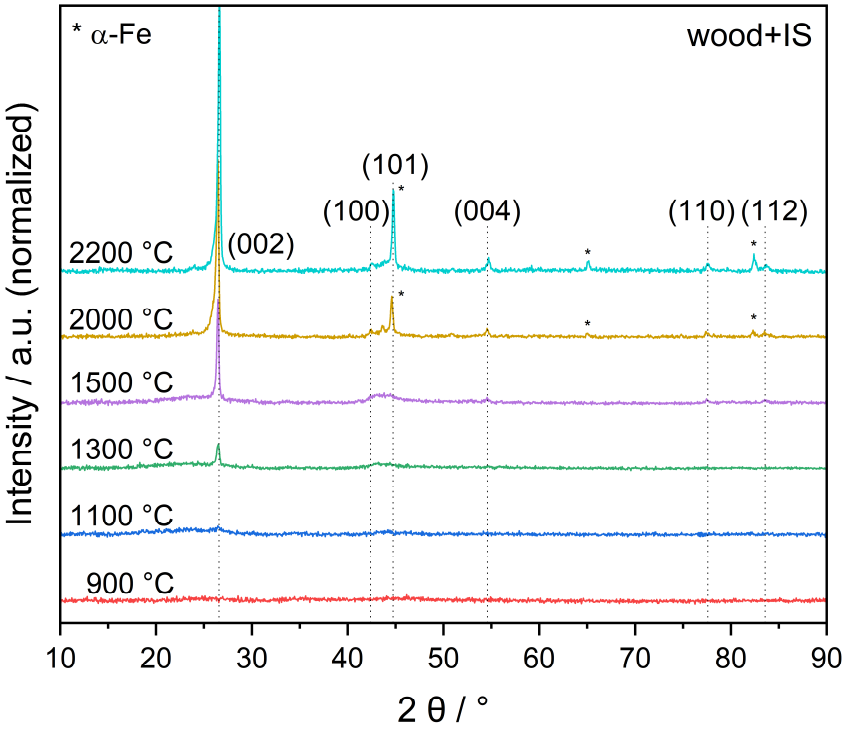


Figure 2. XRD diffractograms of IS-impregnated wood samples at different carbonization temperatures. * indicates peaks originating from Fe impurities.

The value I_{HOR}/I_{LOR} is a parameter for the quantitative amount of graphitic and turbostratic structures relative to amorphous structures. The heigth of the deconvoluted (002) peaks was used for the calculation of this intensity ratio. Figure 3a shows a comparison of I_{HOR}/I_{LOR} at different carbonization temperatures and impregnation conditions. For the impregnated samples, temperature increase leads to an increase in HOR quantity. There is no value for higher temperatures (2000 and 2200 °C) since the (002) peak is very sharp and no LOR peak could be fitted. The non-impregnated samples show HOR peaks at temperatures above 2000 °C, but the ratio of HOR to LOR is low compared to the Fe-impregnated samples. In addition to the number of carbon structures, their quality is assessed too. As displayed in Figure 3b, d_{002} values for HOR and LOR were calculated. The samples carbonized at 900 °C do not exhibit an HOR. We believe that the structures are immature and not fully formed at this stage of carbonization. However, the (002) peak for the iron-impregnated samples at 900 °C is much narrower compared to the reference sample. Therefore, a catalytic effect can be assumed already at this temperature, as described in the literature [23,31]. Starting from 1100 °C, with increasing temperature, a decrease in interlayer spacing within LOR regions can be observed. This means that low-ordered regions become more ordered. However, the most important findings are the interlayer distances of HOR in the iron-impregnated samples. The values are close to the theoretical value of perfect graphite (0.3354 nm), highlighted by a line. In comparison, those of the reference samples are above 0.34 nm, indicating a turbostratic structure for their

HOR. Since wood belongs to the "non-graphitizable" precursors, a turbostratic structure would be expected. It seems possible to surpass this limitation of wood as a precursor by impregnation with iron sulfate salts.

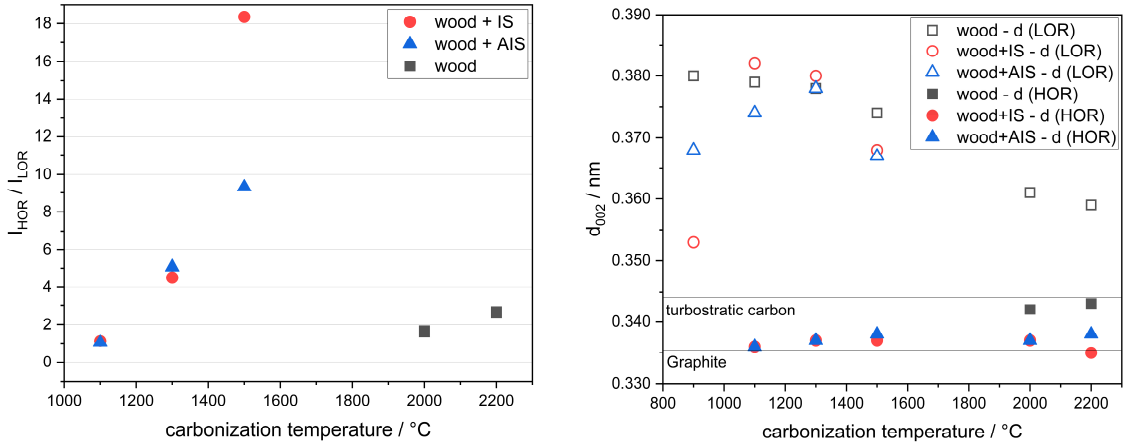


Figure 3. Comparison of (**a**) I_{HOR}/I_{LOR} values for non-impregnated and Fe-impregnated samples at different carbonization temperatures and (**b**) interlayer spacings d_{002} calculated from HOR and LOR peak fittings of different samples at different temperatures.

Calculated XRD values are displayed in Table 1. The crystallite sizes L_c (stacking height) of LOR and HOR structures and subsequently the number of fringes of HOR $n_{fringes}$ were calculated. For the iron-impregnated samples, crystallite sizes at carbonization temperatures higher than 2000 °C are smaller compared to 1500 °C. Since no LOR at higher carbonization temperatures can be detected, we assume that HOR structures are formed out of it. These newly formed graphitic structures possess smaller crystallite sizes, thus reducing the average values. This correlates with the literature findings that graphitic structures are formed around catalyst particles while etching through biomass [21]. Interestingly, at higher temperatures, the iron catalyst seems to be mobile enough to ensure the graphitization of the whole material.

Table 1. Calculated XRD values for non-impregnated and Fe-impregnated samples carbonized at different temperatures.

Sample	d_{002} (LOR)/nm	L_c (LOR)/nm	d_{002} (HOR)/nm	L_c (HOR)/nm	$n_{fringes}$	I_{HOR}/I_{LOR}
wood 900 °C	0.380 ± 0.002	1.06 ± 0.04	x	0	0	0
wood + IS 900 °C	0.353 ± 0.010	1.42 ± 0.08	x	0	0	0
wood + AIS 900 °C	0.368 ± 0.006	1.12 ± 0.10	x	0	0	0
wood 1100 °C	0.379 ± 0.003	1.04 ± 0.04	x	0	0	0
wood + IS 1100 °C	0.382 ± 0.011	1.06 ± 0.10	0.336 ± <0.001	15.59 ± 1.99	47	1.15 ± 0.16
wood + AIS 1100 °C	0.374 ± 0.006	1.09 ± 0.12	0.336 ± <0.001	24.77 ± 0.68	75	1.07 ± 0.13
wood 1300 °C	0.378 ± 0.003	1.07 ± 0.07	x	0	0	0
wood + IS 1300 °C	0.380 ± 0.002	0.93 ± 0.08	0.337 ± 0.001	25.24 ± 0.09	76	4.51 ± 0.83
wood + AIS 1300 °C	0.378 ± 0.005	1.14 ± 0.16	0.337 ± <0.001	34.94 ± 0.64	105	5.07 ± 0.84
wood 1500 °C	0.374 ± <0.001	1.14 ± 0.03	x	0	0	0
wood + IS 1500 °C	0.368 ± 0.005	1.26 ± 0.10	0.337 ± <0.001	34.05 ± 0.01	102	18.35 ± 2.31
wood + AIS 1500 °C	0.367 ± 0.010	1.37 ± 0.29	0.338 ± <0.001	20.20 ± 0.37	61	9.31 ± 3.94
wood 2000 °C	0.361 ± 0.003	1.32 ± 0.08	0.342 ± <0.001	19.52 ± 1.38	58	1.66 ± 0.04
wood + IS 2000 °C	x	0	0.337 ± 0.001	26.61 ± 1.24	80	∞
wood + AIS 2000 °C	x	0	0.337 ± <0.001	15.23 ± 0.72	46	∞
wood 2200 °C	0.359 ± 0.002	1.39 ± 0.04	0.343 ± 0.001	18.00 ± 0.72	54	2.66 ± 0.05
wood + IS 2200 °C	x	0	0.335 ± <0.001	27.96 ± 0.28	84	∞
wood + AIS 2200 °C	x	0	0.338 ± <0.001	23.28 ± 0.97	70	∞

3.2. Raman

Raman spectra are in good agreement with XRD measurements and show an increase in graphitic structure with increasing temperature. However, more information on the structure, texture and nanotexture of the carbonized samples is compiled. Raman spectra are deconvoluted into five peaks in the first-order spectrum in the region between 1000–1800 cm^{-1}, where applicable. Two main peaks, namely the D (~1345 cm^{-1}) and G (~1590 cm^{-1}) bands, are attributed to turbostratic and graphitic carbon nanocrystallites, respectively [43]. The D band is a breathing mode of A_{1g} symmetry and is not possible in perfect graphite. It is therefore characteristic for disorder [44] and structural defects [23]. The G band corresponds to the in-plane E_{2g} optical mode and is characteristic for perfect graphite [45]. The D4 band (~1150 cm^{-1}) is attributed to hydrocarbon or aliphatic moieties connected to graphitic basic structural units [45]. The D3 band (or D" band at ~1500 cm^{-1}) is attributed to amorphous carbon and therefore is of high interest for structural characterization [45]. The D2 band (~1610 cm^{-1}) relates, as the D band, to turbostratic carbon nanocrystallites, representing the edges of a graphitic crystallite [43]. The second-order spectrum in the region between 2400–3300 cm^{-1} reveals bands of lower intensity and is deconvoluted into three further peaks. The G' band (or 2D at ~2650 cm^{-1}) is a Raman-allowed mode for sp^2-carbons and indicates well-stacked graphene layers [40,43]. The other peaks are a G + D band at ~2930 cm^{-1} and 2 D2 band (or 2 D' band) at ~3200 cm^{-1} [43,45], representing the G + D overtone combination and 2 x D2 overtones [23]. Highly oriented pyrolytic graphite reveals a sharp G band, while no D band exists. In the second-order spectrum, a G' band is well established [45]. Other graphite materials show D bands of varying intensities assigned to structural defects [45]. In Figure 4a,b, the structural evolution of non-impregnated and IS-impregnated carbon samples is shown. With increasing temperature, both the D and G band get narrower, meaning lower full width at half maximum (FWHM) values. The sharpened peak at higher temperatures (Figure 4b) reveals shoulders at 1600 cm^{-1}, which indicates turbostratic carbon nanocrystallites. The FWHM of the D band is a parameter used to estimate the disorder degree of polyaromatic stacks [46]. In Figure 5a, the FWHM values of the D bands are shown. With increasing carbonization temperatures, the values decrease. The IS-impregnated samples show less disorder than non-impregnated samples, starting from 1100 °C. This is consistent with XRD measurements, in which impregnated samples at 900 °C show no high-order regions. Using Raman, differences between IS and AIS impregnation can be seen, showing a higher order for the IS-impregnated samples at lower carbonization temperatures. The AIS-impregnated samples show a higher disorder at lower temperatures, until above 1500 °C, polyaromatic stacks become more ordered. The iron-impregnated samples above 2000 °C even show clearly separated D and G bands, revealing the absence of a D3 band, which means the absence of amorphous carbon. The carbon samples above 2000 °C reveal a shoulder at the G band, which is deconvoluted into a D2 band. This is attributed to a higher structural order with subsequent sharper peaks with a lower FWHM. Therefore, the D2 band becomes visible and can be distinguished from the G band. At lower carbonization temperatures, it cannot be distinguished from the G band and is therefore not deconvoluted into a separate peak. With increasing carbonization temperatures and through impregnation with IS and AIS, the D2 band decreases, meaning a less turbostratic and more graphitic structure. This directly corresponds with an increase in the G' band, showing well-stacked graphene layers, mainly through iron impregnation. In the literature, often the D-to-G ratio of peak areas A_D/A_G [43] or peak heights I_D/I_G values [2,40] are shown to demonstrate an increase in graphitic structure. In our case, neither value shows a clear trend, since turbostratic and graphitic structures are both increasing with increasing carbonization temperatures, and therefore, both the D and G band are increasing. Figure 5b shows a comparison of

samples carbonized at 1500 °C. D and G bands are better separated through IS and AIS impregnation. This is attributed to a smaller amount of amorphous carbon, represented by the D3 band at 1500 cm^{-1} and sharper peaks through a higher order. In Figure 6, a comparison of IS-impregnated and non-impregnated wood samples carbonized at 2000 °C is shown. The IS-impregnated sample shows a higher structural order, and the D and the G band are clearly separated. Therefore, no amorphous carbon is detected. This is consistent with the XRD measurements, in which no low-order regions were detected. The D2 band is much smaller, which represents the edges of a graphitic crystallite. This is attributed to larger crystallite sizes. The calculated crystallite size Lc (from XRD measurements) shows 26 nm for the IS-impregnated sample vs. 19 nm for the non-impregnated reference sample (see Table 1). Accordingly, the G' band is larger, showing well-stacked graphene layers. For the non-impregnated wood sample, D4 and D3 bands are clearly visible as well as a more prominent D2 band. To summarize the results from the Raman measurements, impregnation with iron salts led to improved structural development at any carbonization temperature tested within this study when compared to non-impregnated samples.

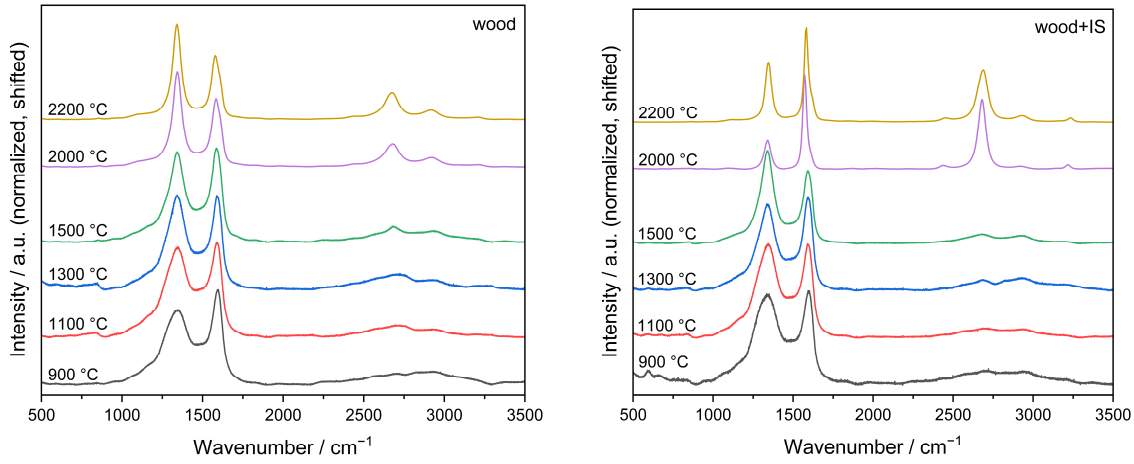


Figure 4. Comparison of (**a**) non-impregnated samples and (**b**) IS-impregnated samples at different temperatures.

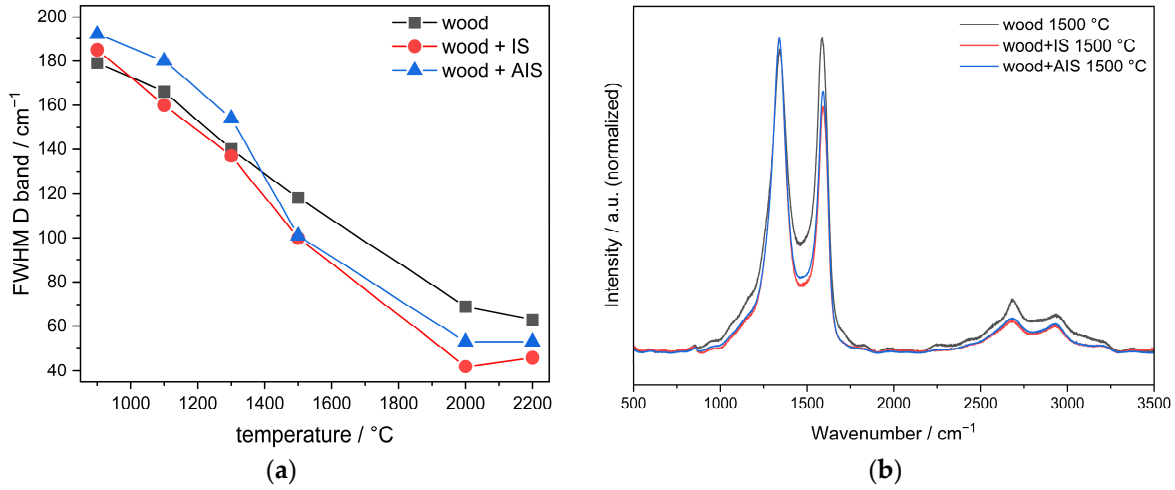


Figure 5. (**a**) FWHM of the D bands of non-impregnated and IS and AIS-impregnated samples at different carbonization temperatures and (**b**) Raman comparison (normalized) of samples carbonized at 1500 °C.

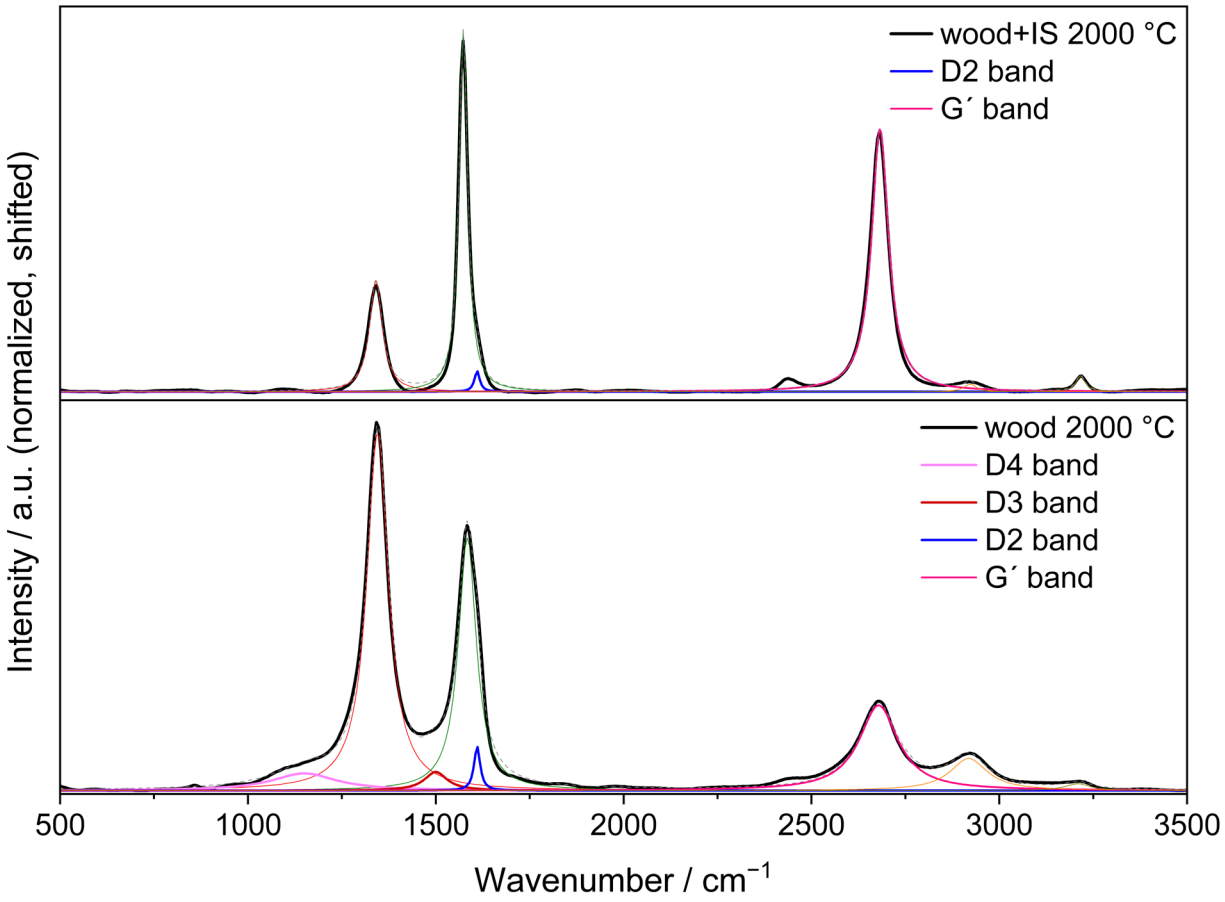


Figure 6. Comparison of IS and non-impregnated wood samples carbonized at 2000 °C, including peak deconvolution. All peaks were fitted but, for the sake of clarity, only relevant peaks were labeled.

3.3. Electrical Resistance

The electrical resistance of the carbonized samples was determined on carbon–PTFE foils using a four-point probe method. As a reference, a similar PTFE foil was prepared from a commercial graphite powder, and the electrical resistance was determined in identical manner. Impregnation with iron salts has an enormous effect on electrical conductivity, as shown in Figure 7a. Especially at a carbonization temperature of 900 °C, values are nearly 100 times lower compared to the non-impregnated samples and prove the catalytic activity of iron at temperatures below 1000 °C, as described in the literature [23,31]. With increasing carbonization temperature, the sheet resistance approaches towards values of the reference foil based on commercial graphite. For the iron-impregnated samples, values in the same range are reached around 1300 °C. According to Krishnan et al., the electrical conductivity of biocarbon increases with increasing graphitic carbon content and through the presence of structural defects [47]. XRD measurements show an increasing graphitic content at higher carbonization temperatures. This is in general agreement with sheet resistance measurements and can explain the lower resistance at higher carbonization temperatures. However, while strong changes can be observed in the XRD data with the complete vanishing of LOR at 2000 °C and above, only minor improvements in electrical conductivity can be observed when increasing the carbonization temperature of the iron-catalyzed samples above 1300 °C. This makes catalytically graphitized biomass highly interesting for electrical applications, as performance competitive to commercial graphite can be achieved at comparatively low temperatures, thus reducing energy input.

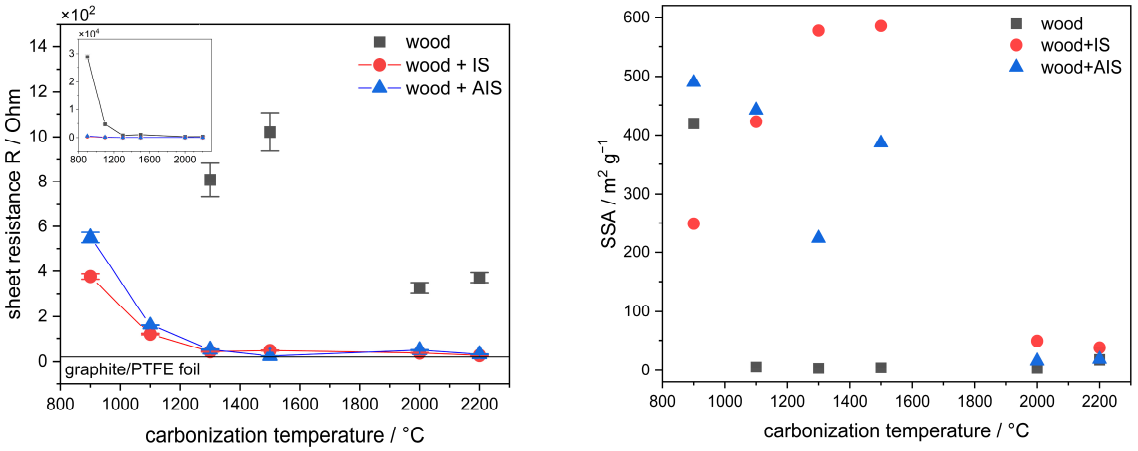


Figure 7. (**a**) Sheet resistance of carbon/PTFE (90/10) foils. As a reference, a graphite/PTFE (90/10) foil is shown. Comparison of iron-catalyzed and non-catalyzed carbon samples at different carbonization temperatures and (**b**) SSA comparison of non-impregnated and Fe-impregnated samples carbonized at different temperatures.

To test the influence of residual iron on electrical conductivity, washed and unwashed iron-impregnated samples carbonized at 1500 °C were compared. The unwashed samples exhibited slightly lower conductivities, which can be attributed to the lower purity of graphite and the higher amount of low-conductivity iron oxides and sulfates that were identified in the XPS analyses (see Table 2).

Table 2. XPS-derived composition of samples carbonized at 1500 °C before (raw) and after washing.

Sample	Composition/at.%			
	C	O	Fe	S
wood 1500 °C	98.11	1.89	0	0
wood + IS 1500 °C	97.67	1.79	0.31	0.24
wood + AIS 1500 °C	97.82	1.53	0.13	0.52
wood + IS 1500 °C (raw)	94.38	4.00	1.29	0.11
wood + AIS 1500 °C (raw)	96.10	2.46	0.81	0.62

The electrical resistance of the non-impregnated samples strongly decreases from 900 to 1300 °C carbonization temperature. At elevated temperatures from 1300 to 2200 °C, only a minor effect on conductivity is observed. The sheet resistance is more than 10 times higher compared to commercial graphite. This is related to the carbon structure, as only turbostratic and no graphitic regions form during the carbonization of the non-impregnated samples.

3.4. Specific Surface Area

Specific surface area (SSA) values were determined from gas adsorption measurements using the BET method (Figure 7b). The SSA for the non-impregnated sample carbonized at 900 °C was 420 m^2 g^{-1}. At higher temperatures, the BET surface area decreases, as described in the literature [48]. Iron-impregnated samples behave differently. While no clear trend is visible among the samples prepared at 900 °C, at higher temperatures, all iron-catalyzed samples show significantly higher surface areas than their non-impregnated counterparts. Thompson et al. describe increased surface areas of iron-catalyzed graphitized wood due to etching of the solid material and an additional small contribution due to the removal of iron residues after acid washing [21].

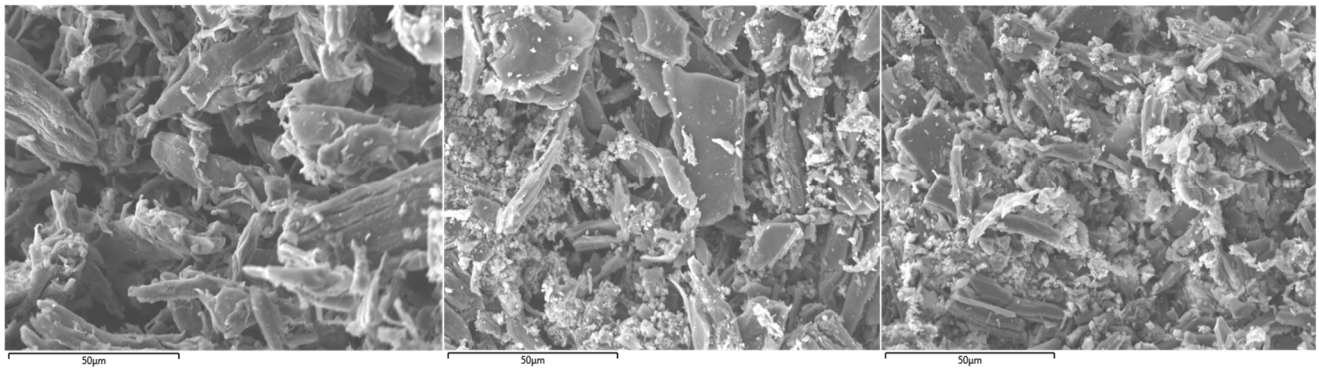
The detailed surface area evolution of the IS- and AIS-impregnated samples with increasing temperatures shows additional trends that are yet not fully understood. The IS-impregnated sample carbonized at 900 °C (wood + IS_900) has a lower SSA of 250 m^2 g^{-1} and increases with increasing carbonization temperature to 423 m^2 g^{-1} at 1100 °C and even 578 and 586 m^2 g^{-1} at 1300 and 1500 °C, respectively. Semeniuk et al. describe an SSA increase in their iron-impregnated sawdust when the carbonization temperature is increased from 700 to 800 °C [27]. They attribute it to an incomplete carbonization reaction at lower temperatures, which leads to the formation of residues, mainly tar, which block the pores. The AIS-impregnated sample carbonized at 900 °C (wood + AIS_900) has a higher SSA of 490 m^2 g^{-1}. The SSA slightly decreases with increasing carbonization temperature, with a much lower value of 225 m^2 g^{-1} at 1300 °C. While the true mechanism is not revealed so far, it could be related to differences in the carbonization behavior in the low temperature range. In contrast to IS, AIS can act as a dehydration catalyst for the cellulosic components of the wood precursor, eventually leading to reduced formation of volatile carbon compounds with increasing temperature [34]. Thus, the maximum surface is already achieved at a lower temperature for the AIS-impregnated sample compared to IS. In addition, XRD and Raman measurements show a large increase in graphitic structure between 1300 and 1500 °C for the AIS-impregnated samples. We attribute this low value to a larger residue formation at 1300 °C due to high catalytic activity at this temperature.

At higher carbonization temperatures, the SSA of both the Fe-catalyzed samples significantly decreases. For the IS-impregnated samples, the SSA decreases to 49 and 38 m^2 g^{-1} for 2000 and 2200 °C, respectively. These values are higher than we would have expected at these carbonization temperatures. The IS-impregnated samples possess a high SSA and pore volume, which, alongside a high degree of graphitization, are important to improve capacitance and rate performance in electrode materials for energy devices [27]. This property profile could make the samples suitable as conductive additives in supercapacitors or electrodes in redox-flow batteries. Above 2000 °C, the SSA values for the AIS-impregnated samples are lower compared to the IS-impregnated samples but still higher than non-impregnated references.

3.5. Morphology and Composition

To examine the morphology and composition of the washed and unwashed samples, SEM-EDX and XPS measurements were conducted. SEM images of unwashed carbons from the impregnated samples show small particles, attributed to iron, attached to the surface of carbonized wood, as shown in Figure 8. The morphology of the carbon particles itself could be described as bulk and slightly lamellar or fibrous due to their higher length in one dimension. No differences in morphology between the non-impregnated and iron-impregnated samples were detected.

After acid washing, most of the iron particles are removed and only small amounts of residual iron remain, as validated by XPS measurements. Since mainly impurities attached to the carbon surface are removed through acid washing, XPS is ideal for checking the residual surface-related impurities. Carbonized samples at 1500 °C were compared to each other after washing, as shown in Table 2. The non-impregnated sample wood at 1500 °C was the purest sample and therefore had the highest carbon content of 98.11 at.% and an oxygen content of 1.89 at.%. For the IS- and AIS-impregnated samples, sulfur and iron were additionally detected, which are attributed to residues of the impregnation salts. The quantities are close to the detection limit, with 0.24 at.% and 0.52 at.% for sulfur and 0.31 at.% and 0.13 at.% for iron, respectively, for IS and AIS. The carbon content ranges between 97.67 at.% and 98.11 at.% for all samples. No major differences in composition can be detected due to the impregnation of the samples.



(**a**) (**b**) (**c**)

Figure 8. SEM pictures of carbonized wood at 900 °C: (**a**) non-impregnated reference sample; (**b**) IS-impregnated sample; (**c**) AIS-impregnated sample.

4. Conclusions

This study demonstrates that iron sulfate salts are effective, scalable and non-toxic catalysts for the graphitization of wood dust. The introduction of these iron salts allows for the formation of high-order regions of the typically "non-graphitizable" wood-based precursor material, with the formation of graphitic regions starting already at temperatures as low as 1100 °C. XRD and Raman spectroscopy confirmed that the Fe-impregnated samples achieved interlayer spacings (d_{002}) as low as 0.335–0.336 nm, which are nearly identical to perfect graphite, whereas the non-impregnated wood reference remained in a turbostratic state even at 2200 °C.

The catalytic effect was further evidenced by the electrical properties of the resulting "biographites". The impregnated samples exhibited electrical resistance values nearly 100 times lower than the reference wood at 900 °C and became competitive with commercial graphite by 1300 °C. Furthermore, the IS-impregnated samples reached a high specific surface area of 586 m^2 g^{-1} at 1500 °C. These combined properties—high graphitic order, low electrical resistance, and potentially high surface area—position these materials as sustainable alternatives to fossil-based synthetic graphite for a large variety of high-performance applications such as batteries, electronics or functional composites upon further optimization regarding purity, particle size and scalability.

Future research will address the residual Fe impurities detected even at higher temperatures, which were likely encapsulated within protective graphitic shells, making them resistant to standard acid washing. Developing more efficient purification techniques or exploring applications where these residual metal particles provide added functionality would be a significant next step. Optimized purification routines in combination with potential catalyst recovery would further improve cost-effectiveness and facilitate industrial implementation. Furthermore, the transfer of the developed technologies to other precursors is ongoing. Impregnation and washing are liquid-based processes without high shear forces. Thus, the use of bio-based fibers or textiles that might allow for the preparation of fibrous or even self-standing textile "biographites" seems very promising. In addition, dedicated use-case-related tests will be essential for validating their commercial and industrial potential as sustainable, bio-based functional materials. This is planned after additional optimization, as higher purity is needed for Li-ion battery anodes, defined sub-micron particles for conductive inks for printed electronics and larger quantities for composite production.

Author Contributions: Conceptualization, S.S. and C.U.; methodology, S.S., R.Z., A.W.H., D.S. and C.U.; software, A.I.M. and R.Z.; validation, S.S., R.Z., N.N., I.A.P. and C.U.; formal analysis, S.S., R.Z. and A.I.M.; investigation, S.S., R.Z., N.N. and I.A.P.; resources, A.W.H., I.A.P., D.S. and C.U.; data curation, S.S., R.Z. and C.F.; writing—original draft preparation, S.S. and C.U.; writing—review and editing, all authors; visualization, S.S. and R.Z.; supervision, D.S. and C.U.; project administration, A.W.H., D.S. and C.U.; funding acquisition, C.F., A.W.H., I.A.P., D.S. and C.U.; All authors have read and agreed to the published version of the manuscript.

Funding: Financial support from the European Regional Development Fund (EFRE) and the province of Upper Austria through the program IBW 2021–2027 (Project Sus2C) is gratefully acknowledged. Further financial support has been obtained through the program THINK.WOOD Innovation funded by the Austrian ministry BMLUK and operated by the FFG (project WOODconduct, FO999893363). Part of this work was performed within the COMET Module Renew4EHS (No. 892416) funded by the Austrian ministries BMIMI, BMWET and the provinces of Upper Austria, Lower Austria and Carinthia (COMET is managed by FFG). I.A.P. acknowledges the support from the Serbian Ministry of Science, Technological Development, and Innovations (contract no. 451-03-34/2026-03/200146) and Serbian Academy of Sciences and Arts (project no. F-49). The financial support for the Christian Doppler Laboratory for Combinatorial Oxide Chemistry by the Christian Doppler Society is gratefully acknowledged.

Data Availability Statement: The original contributions presented in this study are included in the article. Further inquiries can be directed at the corresponding author.

Acknowledgments: The authors used ChatGPT to prepare the Graphical Abstract. The authors manually modified and rearranged the images and added their own figures. The final Graphical Abstract was assembled and revised by the authors. The authors have reviewed and edited the output and take full responsibility for the content of this publication.

Conflicts of Interest: Authors Sabrina Schmid, Neda Nazari, Christian Fürst and Christoph Unterweger were employed by the non-profit research institute Wood K plus—Kompetenzzentrum Holz GmbH that is legally structured as a limited company. The authors declare that the research was conducted in the absence of any commercial or financial relationships that could be construed as a potential conflict of interest. The authors declare that this study received funding from the European Regional Development Fund (EFRE), the province of Upper Austria, the Austrian ministry BMLUK, BMIMI and BMWET (through the FFG), the Serbian Ministry of Science, Technological Development and Innovations, the Serbian Academy of Sciences and Arts and the Christian Doppler Society. The funders were not involved in the study design, collection, analysis, interpretation of data, the writing of this article or the decision to submit it for publication.

References

1. Grohol, M.; Veeh, C. Study on the Critical Raw Materials for the EU 2023: Final Report. Available online: https://op.europa.eu/en/publication-detail/-/publication/57318397-fdd4-11ed-a05c-01aa75ed71a1 (accessed on 10 March 2026).
2. Béguerie, T.; Weiss-Hortala, E.; Nzihou, A. Calcium as an innovative and effective catalyst for the synthesis of graphene-like materials from cellulose. *Sci. Rep.* **2022**, *12*, 21492. [CrossRef] [PubMed]
3. Krishnan, S.G.; White, C.E.; Zeng, K.; Kalarikkal, N.; Ok, Y.S.; Arnold, C.B.; Thomas, S.; Nzihou, A. Recent developments on multi- versus single-metallic catalytic graphitisation of biocarbon: A review. *Fuel* **2025**, *396*, 135330. [CrossRef]
4. Peng, H.; Ming, X.; Pang, K.; Chen, Y.; Zhou, J.; Xu, Z.; Liu, Y.; Gao, C. Highly electrically conductive graphene papers via catalytic graphitization. *Nano Res.* **2022**, *15*, 4902–4908. [CrossRef]
5. Hunter, R.D.; Ramírez-Rico, J.; Schnepp, Z. Iron-catalyzed graphitization for the synthesis of nanostructured graphitic carbons. *J. Mater. Chem. A* **2022**, *10*, 4489–4516. [CrossRef]
6. Rigollet, S.; Weiss-Hortala, E.; Flamant, G.; Nzihou, A. Biocarbon graphenization processes and energy assessment. A review. *Chem. Eng. J.* **2024**, *496*, 153795. [CrossRef]
7. Kane, S.; Storer, A.; Xu, W.; Ryan, C.; Stadie, N.P. Biochar as a Renewable Substitute for Carbon Black in Lithium-Ion Battery Electrodes. *ACS Sustain. Chem. Eng.* **2022**, *10*, 12226–12233. [CrossRef]
8. Banek, N.A.; McKenzie, K.R.; Abele, D.T.; Wagner, M.J. Sustainable conversion of biomass to rationally designed lithium-ion battery graphite. *Sci. Rep.* **2022**, *12*, 8080. [CrossRef] [PubMed]

9. Surovtseva, D.; Crossin, E.; Pell, R.; Stamford, L. Toward a life cycle inventory for graphite production. *J. Ind. Ecol.* **2022**, *26*, 964–979. [CrossRef]
10. Ciacci, L.; de Matos, C.T.; Reck, B.K.; Wittmer, D.; Bernardi, E.; Mathieux, F.; Passarini, F. Material system analysis: Characterization of flows, stocks, and performance indicators of manganese, nickel, and natural graphite in the EU, 2012–2016. *J. Ind. Ecol.* **2022**, *26*, 1247–1260. [CrossRef]
11. Béguerie, T.; Weiss-Hortala, E.; Lyczko, N.; Nzihou, A. The mechanisms of calcium-catalyzed graphenization of cellulose and lignin biochars uncovered. *Sci. Rep.* **2023**, *13*, 11390. [CrossRef] [PubMed]
12. Agrawal, A. Top-down strategies for achieving high-quality graphene: Recent advancements. *J. Ind. Eng. Chem.* **2025**, *142*, 103–126. [CrossRef]
13. Reenu; Sonia; Phor, L.; Kumar, A.; Chahal, S. Electrode materials for supercapacitors: A comprehensive review of advancements and performance. *J. Energy Storage* **2024**, *84*, 110698. [CrossRef]
14. Pandolfo, A.G.; Wilson, G.J.; Huynh, T.D.; Hollenkamp, A.F. The Influence of Conductive Additives and Inter-Particle Voids in Carbon EDLC Electrodes. *Fuel Cells* **2010**, *10*, 856–864. [CrossRef]
15. Kastner, J.; Gnatiuk, I.; Wagner, M.; Holzinger, D.; Rudelstorfer, V.; Hesser, G.; Fuchsbauer, A.; Hild, S. Grinding of nano-graphite inkjet inks for application in organic solar cells. *Nanotechnology* **2019**, *30*, 45601. [CrossRef] [PubMed]
16. Neumaier, L.; Rauter, L.; Zikulnig, J.; Schmid, S.; Unterweger, C.; Pretschuh, C.; Kosel, J. Bio-based carbon as functional material in sustainable printed electronics. *Mater. Lett.* **2026**, *403*, 139424. [CrossRef]
17. Lower, L.; Dey, S.C.; Vook, T.; Nimlos, M.; Park, S.; Sagues, W.J. Catalytic Graphitization of Biocarbon for Lithium-Ion Anodes: A Minireview. *ChemSusChem* **2023**, *16*, e202300729. [CrossRef] [PubMed]
18. Ouzilleau, P.; Gheribi, A.E.; Chartrand, P.; Soucy, G.; Monthioux, M. Why some carbons may or may not graphitize?: The point of view of thermodynamics. *Carbon* **2019**, *149*, 419–435. [CrossRef]
19. Chen, C.; Sun, K.; Huang, C.; Yang, M.; Fan, M.; Wang, A.; Zhang, G.; Li, B.; Jiang, J.; Xu, W.; et al. Investigation on the mechanism of structural reconstruction of biochars derived from lignin and cellulose during graphitization under high temperature. *Biochar* **2023**, *5*, 77. [CrossRef]
20. Thompson, M.; Xia, Q.; Hu, Z.; Zhao, X.S. A review on biomass-derived hard carbon materials for sodium-ion batteries. *Mater. Adv.* **2021**, *2*, 5881–5905. [CrossRef]
21. Thompson, E.; Danks, A.E.; Bourgeois, L.; Schnepp, Z. Iron-catalyzed graphitization of biomass. *Green Chem.* **2015**, *17*, 551–556. [CrossRef]
22. Nakayasu, Y.; Goto, Y.; Katsuyama, Y.; Itoh, T.; Watanabe, M. Highly crystalline graphite-like carbon from wood via low-temperature catalytic graphitization. *Carbon Trends* **2022**, *8*, 100190. [CrossRef]
23. Hoekstra, J.; Beale, A.M.; Soulimani, F.; Versluijs-Helder, M.; Geus, J.W.; Jenneskens, L.W. Base Metal Catalyzed Graphitization of Cellulose: A Combined Raman Spectroscopy, Temperature-Dependent X-ray Diffraction and High-Resolution Transmission Electron Microscopy Study. *J. Phys. Chem. C* **2015**, *119*, 10653–10661. [CrossRef]
24. Hunter, R.D.; Rowlandson, J.L.; Smales, G.J.; Pauw, B.R.; Ting, V.P.; Kulak, A.; Schnepp, Z. The effect of precursor structure on porous carbons produced by iron-catalyzed graphitization of biomass. *Mater. Adv.* **2020**, *1*, 3281–3291. [CrossRef]
25. Yan, Q.; Zhang, X.; Li, J.; Hassan, E.B.; Wang, C.; Zhang, J.; Cai, Z. Catalytic conversion of Kraft lignin to bio-multilayer graphene materials under different atmospheres. *J. Mater. Sci.* **2018**, *53*, 8020–8029. [CrossRef]
26. Romero Millán, L.M.; Ghogia, A.C.; White, C.E.; Nzihou, A. Iron Nanoparticles to Catalyze Graphitization of Cellulose for Energy Storage Applications. *ACS Appl. Nano Mater.* **2023**, *6*, 3549–3559. [CrossRef]
27. Semeniuk, M.; Sarshar, Z.; Gezahegn, S.; Li, Z.; Egbedina, A.; Tjong, J.; Oksman, K.; Chin, Y.-H.; Sain, M. Catalytically transformed low energy intensive 2D-layered and single crystal-graphitic renewable carbon cathode conductors. *Carbon* **2021**, *183*, 243–250. [CrossRef]
28. Kubo, S.; Uraki, Y.; Sano, Y. Catalytic graphitization of hardwood acetic acid lignin with nickel acetate. *J. Wood Sci.* **2003**, *49*, 188–192. [CrossRef]
29. Chen, C.; Sun, K.; Wang, A.; Wang, S.; Jiang, J. Catalytic Graphitization of Cellulose Using Nickel as Catalyst. *BioResources* **2018**, *13*, 3165–3176. [CrossRef]
30. Yan, Q.; Li, J.; Zhang, X.; Hassan, E.B.; Wang, C.; Zhang, J.; Cai, Z. Catalytic graphitization of kraft lignin to graphene-based structures with four different transitional metals. *J. Nanopart Res.* **2018**, *20*, 1861. [CrossRef]
31. Lempiäinen, H.; Bergna, D.; Heponiemi, A.; Hu, T.; dos Reis, G.S.; Sliz, R.; Lassi, U. Fe-based catalytic modification of a birch sawdust-based carbon structure: The effect of process parameters on the final product using an experimental design. *Carbon Trends* **2024**, *17*, 100428. [CrossRef]
32. Hunter, R.D.; Takeguchi, M.; Hashimoto, A.; Ridings, K.M.; Hendy, S.C.; Zakharov, D.; Warnken, N.; Isaacs, J.; Fernandez-Muñoz, S.; Ramirez-Rico, J.; et al. Elucidating the Mechanism of Iron-Catalyzed Graphitization: The First Observation of Homogeneous Solid-State Catalysis. *Adv. Mater.* **2024**, *36*, e2404170. [CrossRef] [PubMed]
33. Ōya, A.; Marsh, H. Phenomena of catalytic graphitization. *J. Mater. Sci.* **1982**, *17*, 309–322. [CrossRef]

34. Unterweger, C.; Schlapp-Hackl, I.; Fürst, C.; Robertson, D.; Cho, M.; Hummel, M. Carbon Fibers Based on Cellulose–Lignin Hybrid Filaments: Role of Dehydration Catalyst, Temperature, and Tension during Continuous Stabilization and Carbonization. *Fibers* **2024**, *12*, 55. [CrossRef]
35. Liu, J.; Sun, J.; Huang, X.; Li, G.; Liu, B. Goldindec: A Novel Algorithm for Raman Spectrum Baseline Correction. *Appl. Spectrosc.* **2015**, *69*, 834–842. [CrossRef] [PubMed]
36. Breitenbach, S.; Duchoslav, J.; Mardare, A.I.; Unterweger, C.; Stifter, D.; Hassel, A.W.; Fürst, C. Comparative Behavior of Viscose-Based Supercapacitor Electrodes Activated by KOH, H_2O, and CO_2. *Nanomaterials* **2022**, *12*, 677. [CrossRef] [PubMed]
37. Valdes, L. Resistivity Measurements on Germanium for Transistors. *Proc. IRE* **1954**, *42*, 420–427. [CrossRef]
38. Gomez-Martin, A.; Schnepp, Z.; Ramirez-Rico, J. Structural Evolution in Iron-Catalyzed Graphitization of Hard Carbons. *Chem. Mater.* **2021**, *33*, 3087–3097. [CrossRef]
39. Puech, P.; Dabrowska, A.; Ratel-Ramond, N.; Vignoles, G.L.; Monthioux, M. New insight on carbonisation and graphitisation mechanisms as obtained from a bottom-up analytical approach of X-ray diffraction patterns. *Carbon* **2019**, *147*, 602–611. [CrossRef]
40. Rigollet, S.; Béguerie, T.; Weiss-Hortala, E.; Flamant, G.; Nzihou, A. Synthesis of graphitic biocarbons from lignin fostered by concentrated solar energy. *Sci. Rep.* **2025**, *15*, 6418. [CrossRef] [PubMed]
41. Monthioux, M. Describing carbons. *Carbon Trends* **2024**, *14*, 100325. [CrossRef]
42. Ngene, G.I.; Nzihou, A. Catalytic conversion of spent coffee grounds into graphitic and nanotube biocarbon. *Mater. Today Commun.* **2025**, *47*, 113240. [CrossRef]
43. Enengl, C.; Lumetzberger, A.; Duchoslav, J.; Mardare, C.C.; Ploszczanski, L.; Rennhofer, H.; Unterweger, C.; Stifter, D.; Fürst, C. Influence of the carbonization temperature on the properties of carbon fibers based on technical softwood kraft lignin blends. *Carbon Trends* **2021**, *5*, 100094. [CrossRef]
44. Ferrari, A.C.; Robertson, J. Interpretation of Raman spectra of disordered and amorphous carbon. *Phys. Rev. B* **2000**, *61*, 14095–14107. [CrossRef]
45. Bokobza, L.; Bruneel, J.-L.; Couzi, M. Raman Spectra of Carbon-Based Materials (from Graphite to Carbon Black) and of Some Silicone Composites. *C* **2015**, *1*, 77–94. [CrossRef]
46. Ishimaru, K.; Hata, T.; Bronsveld, P.; Meier, D.; Imamura, Y. Spectroscopic analysis of carbonization behavior of wood, cellulose and lignin. *J. Mater. Sci.* **2007**, *42*, 122–129. [CrossRef]
47. Krishnan, S.G.; Bose, B.A.; Kalarikkal, N.; Thomas, S.; Nzihou, A. Effect of Structural Defects on Electrical Conductivity of Graphitic Biocarbon. *ACS Omega* **2025**, *10*, 45323–45333. [CrossRef] [PubMed]
48. Buiel, E.R.; George, A.E.; Dahn, J.R. Model of micropore closure in hard carbon prepared from sucrose. *Carbon* **1999**, *37*, 1399–1407. [CrossRef]

Disclaimer/Publisher's Note: The statements, opinions and data contained in all publications are solely those of the individual author(s) and contributor(s) and not of MDPI and/or the editor(s). MDPI and/or the editor(s) disclaim responsibility for any injury to people or property resulting from any ideas, methods, instructions or products referred to in the content.